Resonant passive energy balancing for a morphing helicopter blade

Jiaying Zhang [a,b,*], Alexander D. Shaw [c], Chen Wang [d], Huaiyuan Gu [e], Mohammadreza Amoozgar [f], Michael I. Friswell [c]

[a] *School of Aeronautic Science and Engineering, Beihang University, Beijing 100191, China*
[b] *Ningbo Institute of Technology, Beihang University, Ningbo 315800, China*
[c] *College of Engineering, Swansea University, Swansea SA2 8PP, United Kingdom*
[d] *College of Aerospace Engineering, Nanjing University of Aeronautics and Astronautics, Nanjing 210016, China*
[e] *University of Bristol, Bristol, England BS8 1TR, United Kingdom*
[f] *Department of Mechanical, Materials and Manufacturing Engineering, University of Nottingham, NG7 2RD, United Kingdom*

A B S T R A C T

The idea of morphing a helicopter blade by using compliant structures promises augmented capabilities in terms of manoeuvrability and fuel efficiency. To achieve morphing, compliant structures work by elastically deforming to achieve the desired response, and therefore actuation must work against the inherent structural stiffness in addition to external loads. Passive Energy Balancing has previously addressed this problem for quasistatic loads, by adding negative stiffness elements in parallel with the structural stiffness, so that stiffness is reduced almost to zero and lighter actuators may be used. This work extends this idea to the case of dynamic actuation, where negative stiffness is optimally used to reduce the natural frequency of a morphing blade, so that it may resonate at the desired actuation frequency. A negative stiffness mechanism in parallel with the structural stiffness can be used to tailor the natural frequency of a morphing blade system. Furthermore, the negative stiffness mechanism introduces nonlinearity that has some benefits in stabilising the resonant response amplitude compared to a linear resonance, and is also shown to be beneficial to achieve a weight efficient mechanism. A spiral pulley negative stiffness mechanism has previously addressed this problem for quasistatic loads and is extended here to achieve linear frequency tailoring and nonlinear frequency tailoring, respectively. The equivalent stiffness of the extended spring used in the rotating system has been investigated. Resonant morphing strategies exploiting dynamic tailoring have been studied showing encouraging preliminary results.

© 2022 Elsevier Masson SAS. All rights reserved.

1. Introduction

Nowadays, morphing technology can significantly reduce the mass and energy consumption, and improve the overall flight performance compared to traditional aircraft structures, and hence they are receiving widespread interest across the aerospace industry [1–10]. Advances in the development of smart actuators and compliant structures have made morphing wings become feasible. The aircraft system can therefore be integrated to allow shape changes of the structure, and therefore adapt its aerodynamic properties to suit changing requirements. Compared with morphing technology used in fixed wing aircraft, morphing rotorcraft blades promise improved performance by changing their aerodynamic characteristics by a continuous change in shape. Rotorcraft use cyclic pitch control for tuning the lift when the blades rotate,

since the blades need to be pitched once-per-revolution to avoid large rolling moments as the incident flow velocity varies for different azimuth angles [11,12]. The lift the blade generates on the retreating side therefore limits the maximum speed of the rotorcraft. Consequently, the performance of the rotor and the stability of the helicopter will be reduced. In order to improve rotor performance, considerable research has investigated morphing structure concepts. The idea of morphing blades by using compliant structures promises augmented capabilities in terms of manoeuvrability and fuel efficiency [13–16].

In previous studies, a novel concept of dynamic stall control for rotor aerofoil via a variable droop leading-edge (VDLE) has been investigated [17,18]. The variable droop leading edge is used to suppress the dynamic stall vortex of the aerofoil and improve the performance during dynamic stall. The maximum drag and negative moment coefficients can be reduced by about 79.2% and 81.2% respectively. Moreover, the lift of an aerofoil depends on its chord length and blade surface area, and chord extension morphing of

* Corresponding author.
E-mail address: jiaying.zhang@buaa.edu.cn (J. Zhang).

Nomenclature

α	pitch angle	I	second moment of area of the morphing camber
d	magnitude of camber morphing	ρ	Mass density of morphing camber spine
b	semi-length of the rigid segment	c	damping constant
c	chord	δ	spiral pulley rotation angle
m	mass of the nonlinear mass-spring-damper system	θ	associated offset angle of spiral pulley
c_s	damping coefficient of the nonlinear mass-spring-damper system	δ_0	initial pulley rotation angle of the spiral pulley
		r_0, k_1, k_2	parameters of the spiral profile
k_s	stiffness of the nonlinear mass-spring-damper system	L_0	Initial extended spring length
k_{n1}	linear coefficient of a negative stiffness device	K	spring constant
k_{n3}	cubic coefficient of a negative stiffness device	$\rho_s A_s$	mass per unit length of the spring
y_{ten}	tendon mounting offset	$E_s A_s$	effective axial stiffness of the spring
k_{ten}	stiffness of the tendon	l_h	offset position of the spring
r_f	spooling pulley radius	u_s	deformation of the spring caused by centrifugal force
x_l	negative stiffness mounting point	l_s	initial length of the spring
l	length of the morphing camber segment	k_ω	equivalent stiffness of the spring under rotation
E	Young's modulus of the morphing camber		

helicopter rotors has been shown to be highly beneficial for stall alleviation [13,19]. Some other concepts for morphing blades focus on camber change and active twist; compliant structures have been used as an alternative to trailing-edge flaps [20,21] and composite structures have been used to modify the twist and the torsional stiffness of rotating blades [22–24].

A typical morphing system is composed of light and compliant materials and is driven by traditional actuators, such as electromechanical actuation [25]. Some of these actuators, such as piezoelectric actuators, are compact, high-force and high bandwidth devices, but they can only provide a limited stroke. Frequently the use of these actuators to drive the system can cost noteworthy energy for each cycle of operation and the spent energy cannot be recovered. This limitation can be critical in cases where large operation or large-size rotor blades are needed. Therefore, there is increasing interest in resonant actuation, particularly in aerospace engineering. Resonant actuation alters a structure to ensure that the inertia and stiffness forces cancel each other out in a desired actuation cycle, thereby minimising the demand on actuators. An N-link snake robot with parallel elastic actuators (PEA) was investigated and the spring stiffness was chosen to achieve resonant actuation [26]. With the optimised spring stiffness, the PEA reduced the current consumption by 72% during the fast movement of the robot [26]. Moreover, resonant actuation can be potentially applied to morphing. Piezoelectric resonant actuation systems for an active flap of helicopter rotors have been investigated by tailoring the natural frequencies of the actuation system to the required operating frequencies to increase the output authority. Numerical simulations reveal that the actuator authority at the tuned frequency can be increased with wide operating bandwidths compared to the original actuation system without resonant tuning [27,28]. For the morphing application, a bistable wing has been investigated using surface bonded piezoelectric materials, exploiting resonance to achieve snap-through of the structure with lower excitation voltage [29,30]. Moreover, an elastic ring with a compliant mechanism has been designed to achieve resonant wing actuation mechanism for application in flapping wing MAVs, so that the wing reduces the energy expenditure and provides amplitude amplification [31].

A promising active camber morphing concept for rotorcraft and fixed wing aircraft has been proposed, known as the Fish Bone Active Camber (FishBAC) [32–35], which uses a biologically inspired internal bending beam and elastomeric matrix composite as the skin surface. Passive energy balancing has been previously investigated to reduce actuation requirements for quasistatic loads, by adding negative stiffness elements in parallel with the structural

stiffness, so that stiffness is reduced almost to zero and lighter actuators may be used [36–38]. This work extends this idea to the case of dynamic actuation for morphing structure applications, where negative stiffness is optimally used to reduce the natural frequency of the morphing blade so that it can resonate at a desired actuation frequency.

Fig. 1 shows the integration of passive energy balancing for morphing blades with a fixed speed of the rotor. The spiral pulley negative stiffness mechanism has been arranged along the spanwise direction of the morphing blade. The morphing will be operated at one cycle per revolution, so that the operating frequency is fixed. Therefore, the negative stiffness mechanism can be designed to tailor the natural frequency of the blade to generate resonance.

A numerical investigation of a 2D harmonically morphed rotor airfoil during a pitching motion has been undertaken by Komp et al. [39,40], where the reference Bo 105 rotor operates at 420 RPM (7 Hz). The rotor blades undergo the usual cyclic pitching motion $\alpha(t)$, with an additional time-varying magnitude of camber morphing $d(t)$. The harmonic motion is described by

$$\begin{aligned} \alpha(t) &= \alpha_{mean} + \alpha_{hpp}\sin(2\pi t f_\alpha) \\ d(t) &= d_{mean} + d_{hpp}\sin(2\pi t f_d + \varphi_d), \end{aligned} \tag{1}$$

where α is the mean pitch amplitude and d is the vertical trailing-edge tip deflection, φ_d is the initial phase shift and f_α and f_d are the actuation frequencies of the pitch cycle and the morphing camber, and are equal to the rotor frequency.

The resulting time-histories of airfoil pitch and the resultant trailing edge tip deflection profiles are illustrated in Fig. 2. This led to the change in thrust distribution shown in Fig. 3. The rotor thrust is increased on the retreating side due to the camber deflection, resulting in increased loading on the lateral sides of the rotor disk and a decrease over the front and aft sections. Therefore, a harmonically morphed rotor aerofoil during the pitching cycle over a rotor revolution can significantly improve rotor efficiency.

This work extends the work on harmonically morphed rotor aerofoils by developing means to incorporate negative stiffness into the system for dynamic tailoring, a process we refer to as Resonant Passive Energy Balancing. While this is a similar idea to the quasistatic Passive Energy Balancing presented previously, the objective is now to facilitate resonance with a negative stiffness mechanism, rather than simply drive stiffness to near zero as in the quasistatic case.

The effect of simple passive energy balancing with an assumed cubic stiffness applied to a classical mass-spring-damper system is
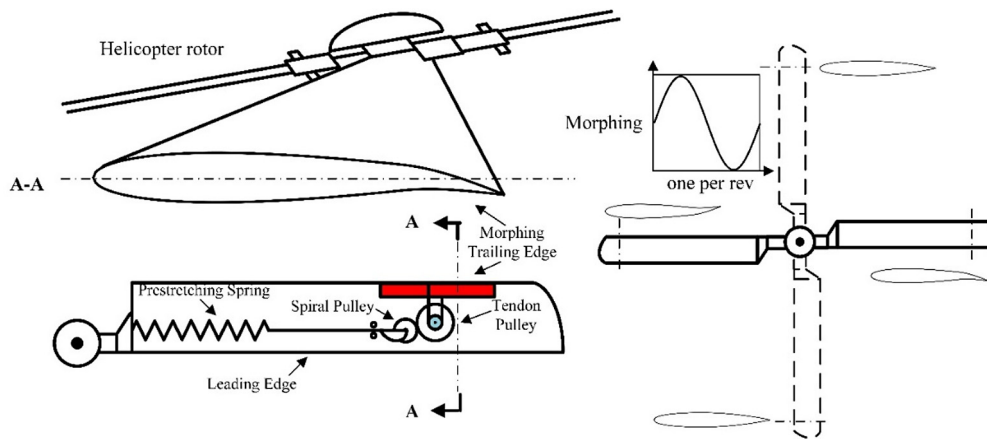
Fig. 1. Schematic showing integration of passive energy balancing for morphing blades. The prestretched spring, spiral pulley, and bevel gear are integrated into leading edge of blades and morphing is operated at once per rev.
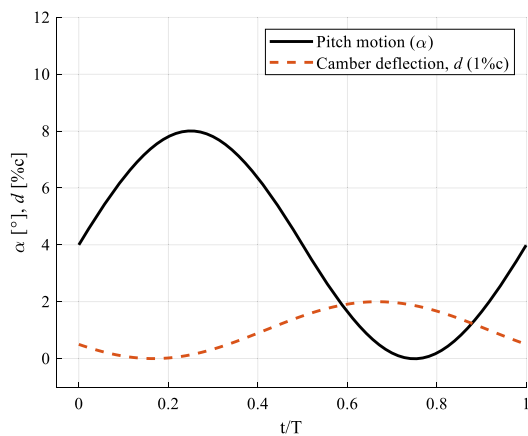

Fig. 2. Example pitching motion and morphing actuation profile over a pitch period [41].

presented first. It is shown that the nonlinearity has two important benefits; firstly, it restricts the amplitude that can be reached at a fixed forcing frequency, unlike a linear resonance which can lead to dangerously high amplitudes. Secondly, it can be shown that allowing some nonlinearity reduces the amount of stored elastic energy required for the negative stiffness mechanism, and this leads to lower mass. Then, the case of a camber morphing blade is considered. In order to analyse the dynamic tailoring of a morphing camber by using negative stiffness, a spiral pulley negatives stiffness mechanism is chosen to provide different cases for stiffness tailoring. Finally, the morphing camber is investigated using a cantilever beam to represent the trailing edge structure of the blade. To achieve dynamic tailoring, the spiral pulley negative stiffness mechanism is parameterised to trim the stiffness of the morphing camber. Elastic beam theory is used to describe its behaviour and a linear negative stiffness element is considered. Then, a nonlinear negative stiffness mechanism is used to provide more stability and reduced energy storage to the morphing camber blade. The results show that the dynamic behaviour of the morphing camber can be tailored by using a negative stiffness mechanism, resulting in significant reductions in required actuation power.

2. Forced oscillations with nonlinear response

Previous works [36–38] have considered the use of Passive Energy Balancing for elastic, quasistatic applications. This section will consider how the design of the Passive Energy Balancer (PEB) changes, when the dynamic forces of inertia and damping are con-

sidered. A PEB mechanism consisting of an assumed cubic stiffness is applied to a classical mass-spring-damper system, hence incorporating inertia, damping and nonlinearity in the simplest possible way. This is then used to highlight the ways our view of PEB changes when these dynamic terms are considered, and develop the concept of Resonant Passive Energy Balancing.

Fig. 4 shows the system under consideration. The equation of motion of this system can be rewritten as

$$f_a(t) = m\ddot{x} + c_s\dot{x} + k_s x + k_{n1}x + k_{n3}x^3 \tag{2}$$

where $f_a(t)$ is the force provided by the actuator, and m, c_s and k_s are respectively the mass, damping coefficient and stiffness assigned to the structure that we wish to actuate. The terms k_{nl} and k_{n3} are the linear and cubic coefficients of a negative stiffness device attached in parallel to the structure, in order to reduce the overall stiffness that the actuator must work against. In principle, the spiral pulley device is able to produce arbitrary force-displacement characteristics. However, smooth characteristics are preferred to ensure the pulley geometry may be manufactured easily; hence the use of low degree polynomials. A quadratic stiffness term is avoided to ensure symmetry in the nonlinear stiffness.

For simplicity, the motion of the mass is prescribed to be

$$x(t) = X\cos(\Omega t) \tag{3}$$

where Ω is the angular frequency of operation. Therefore, by substituting Eq. (3) into Eq. (2) we obtain

$$f_a(t) = \left(-\Omega^2 m + k_s + k_{n1} + \frac{3}{4}k_{n3}X^2\right)X\cos\Omega t$$
$$- c_s\Omega X\sin\Omega t + \frac{1}{4}k_{n3}X^3\cos 3\Omega t \tag{4}$$

The instantaneous power exerted by the actuator on the mass is given by

$$p_i = f_a\dot{x} \tag{5}$$

which on substitution of Eqs. (3) and (4) becomes

$$p_i = \frac{\Omega X^2}{2}\left[-\left(-\Omega^2 m + k_s + k_{n1} + \frac{1}{2}k_{n3}X^2\right)\sin 2\Omega t\right.$$
$$\left. + c_s\Omega(1 - \cos 2\Omega t)\right] - \frac{k_{n3}\Omega X^4}{8}\sin 4\Omega t \tag{6}$$

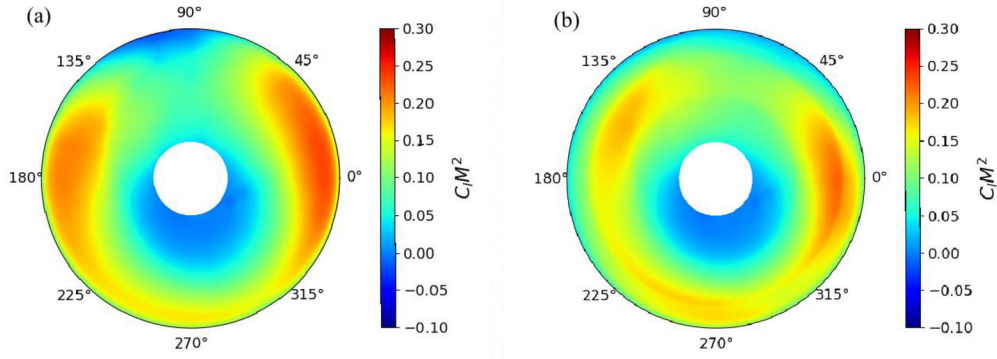Alternatively, we could consider the average power exerted upon the mass given by

Fig. 3. Polar plots illustrating the rotor thrust from active camber actuation (a) baseline (b) active camber [40].
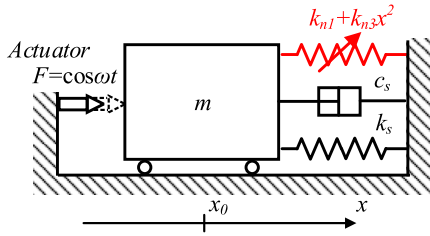

Fig. 4. The single degree of freedom model of the nonlinear mass-spring-damper system.

$$\overline{p}_i = \frac{\Omega}{2\pi} W_0 \qquad (7)$$

where W_0 is the work per actuation cycle given by

$$W_0 = \oint f_a dx = \int_0^T f_a \dot{x} dt = \int_0^T p_i dt \qquad (8)$$

where $T = 2\pi/\Omega$ is the period of actuation. Evaluating Eq. (8) with Eq. (6) substituted, it is clear that the integrals of all trigonometric terms are zero, leaving

$$W_0 = \pi c_s \Omega X^2 \qquad (9)$$

This result suggests that passive energy balancing will not affect the average power consumption of the actuator. However, this ignores the fact that most actuators are not regenerative, meaning that they do not recover energy, and therefore do not perform negative work when p_i is negative. In fact, Eq. (9) shows the minimum possible work per cycle, or in other words the proportion of work that cannot possibly be reduced by passive energy balancing. To get a more reasonable estimate of work or power, we need to ensure that when the instantaneous power is negative, the resulting energy is simply dissipated and is not available for useful effort later. To capture this effect in the simplest way we simply zero any negative power, and hence we can define the Positive Instantaneous Power (PIP) function as follows:

$$p_+ = \begin{cases} p_i, & p_i > 0 \\ 0, & p_i \leq 0 \end{cases} \qquad (10)$$

This leads to the positive work over a cycle by modifying Eq. (8) to give

$$W_+ = \int_0^T p_+ dt \qquad (11)$$

Note that W_+ could be found by integrating p_i and excluding any negative regions from the integral. This can be approximately solved by neglecting the 4Ω harmonic term and time shifting the solution to get p_i in the form $p_i = P\cos 2\Omega t + P_0$. Symmetry and periodicity can then be exploited to obtain

$$W_+ \approx 4 \int_0^{t^*} p_i dt = 2\left(\frac{P}{\Omega}\sin\left(2\Omega t^*\right) + 2P_0 t^*\right) \qquad (12)$$

where

$$P = \frac{\Omega X^2}{2}\sqrt{\left(-\Omega^2 m + k_s + k_{n1} + \frac{3}{4}k_{n3}X^2\right)^2 + (c_s\Omega)^2 P_0}$$

$$= \frac{c_s\Omega^2 X^2}{2} \qquad (13)$$

and t^* is the time from the maximum instantaneous power to the zero crossing of p_i, or to the minimum of p_i if there is no zero crossing, given by

$$t^* = \begin{cases} \cos^{-1}(-P_0/P)/2\Omega, & P > P_0 \\ \pi/2\Omega, & P \leq P_0 \end{cases} \qquad (14)$$

For further insight, let us assume a nondimensional system, where $m = k_s = X = 1$ and $c_s = 0.2$, hence the underlying system has a natural frequency of $\omega_n = \sqrt{k_s/m} = 1$ and a damping ratio of $\xi = \frac{c_s}{2\sqrt{k_s m}} = 0.1$. Let us also imagine that we wish to actuate this system at $\Omega_0 = 0.5$, i.e. at half its natural frequency. In order to achieve resonant actuation at our chosen frequency Ω_0, we choose k_{n1} and k_{n3} to zero the effective linear stiffness in Eq. (4), i.e.

$$-\Omega_0^2 m + k_s + k_{n1} + \frac{3}{4}k_{n3}X^2 = 0 \qquad (15)$$

For an initial demonstration, let us consider when Eq. (15) is solved by $k_{n1} = -0.9$ and $k_{n3} = 0.2$.

Fig. 5 shows the actuator work per cycle of a nondimensional system, compared to a system with a PEB optimised for actuation at half the natural frequency, showing that there are substantial power savings at all frequencies up to and slightly beyond the target frequency. The performance is however limited by the system damping. It shows that the Resonant Passive Energy Balancing will provide substantial power savings at this frequency and below. Unsurprisingly, as we progress to frequencies above our chosen resonance, the performance rapidly deteriorates until it is poorer than the unassisted system. This is the region where dynamic actuation forces are dominated by inertia and hence stiffness reduction is of no benefit.
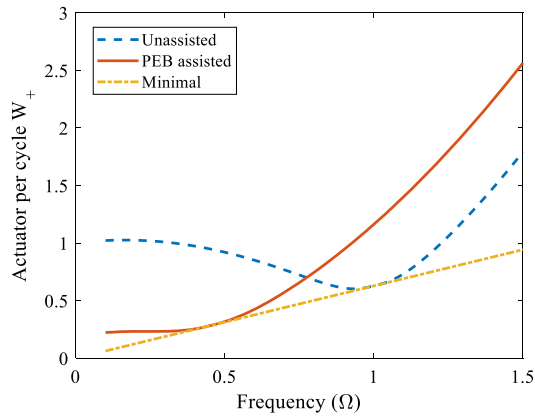
Fig. 5. Work per cycle of a nondimensional linear system at different frequencies, compared with a system with a PEB optimised for actuation at frequency $\Omega_0 = \omega_n/2$. The lower (minimal) line shows the work predicted by Eq. (14).
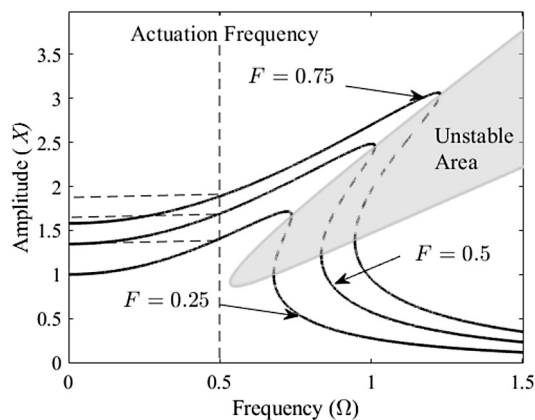

Fig. 6. The amplitude-frequency characteristic curves.

The response sensitivity of a nonlinear system can be studied by considering the forced system

$$m\ddot{x} + c_s\dot{x} + k_s x + k_{n1}x + k_{n3}x^3 = F\cos\Omega_0 t \tag{16}$$

and assuming that $x(t) = X\cos(\Omega_0 t + \varphi)$. The relationship between the system parameters and the external force amplitude is

$$\left(\left(k_s - \Omega_0^2 m\right) + k_{n1} + \frac{3}{4}k_{n3}X^2\right)^2 + (c_s\Omega_0)^2 = \frac{F^2}{X^2} \tag{17}$$

Since we want a hardening nonlinear response, we know that $\frac{3}{4}k_{n3}X^2$ is a positive term. Fig. 6 shows the frequency-response curve for different actuation amplitude F for the single degree of freedom model. It can be seen that the nonlinearity provides a hardening stiffness for the system, i.e. $k_{n3} > 0$. As such nonlinearity can prevent excessive change of response amplitude if the actuation amplitude is changed, which ensures the output is within a reasonable range. For example, if the system is designed to produce an output $X = 1.6$ and under an actuation frequency of 0.5 with amplitude $F = 1.6$, even if the actuation amplitude changed by 50%, the variation in output amplitude is less than 10%, as shown in Fig. 6. This means that a nonlinear resonance can be far more consistent in its response than a linear one, in the presence of uncertainty regarding excitation amplitude and damping.

Unfortunately, a nonlinear system can also introduce unpredictability into the response in the form of multiple responses to harmonic forcing between the jump up and dropdown frequencies [42]. This presents a difficulty for the nonlinear resonant actuation concept, as the risk of losing resonance and receiving much
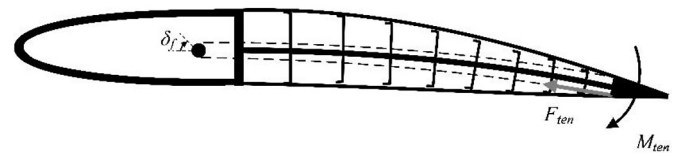

Fig. 7. Schematic of the morphing camber model, δ_f is rotation angle of spooling pulley to produce a moment at the trailing edge.

lower response amplitude would be unacceptable. However, Fig. 6 also shows that there is a region of substantial resonance near the assumed actuation frequency that avoids this problem, so long as the response does not stray too far into the region of highly stiffened nonlinear response. Indeed the nonlinearity and actuation frequency should be carefully chosen to avoid multiple solutions and unstable responses.

3. Morphing camber with a negative stiffness mechanism

3.1. The morphing camber model

Resonant Passive Energy Balancing has been demonstrated theoretically for a classical mass-spring-damper system in Section 2. This section extends the concept to a morphing camber section. The negative stiffness mechanism will be investigated with both linear negative stiffness and nonlinear negative stiffness. The morphing concept known as the fish bone active camber (FishBAC) [21] is chosen as the target structure for study. Fig. 6 shows schematically the forces and moments generated by the tendons due to pulley rotation, the corresponding magnitudes of which have been derived in [32].

Fig. 7 shows the morphing camber model that consists of two chord segments, the front segment is a non-morphing D spar and the rear segment is a biologically inspired compliant structure. The rear segment is clamped to the non-morphing D spar that can be considered rigid. Therefore, the rear segment can be considered as a cantilever beam and elastic beam theory is used to describe its behaviour as shown in Fig. 8. The rear segment is actuated by the tendons attached to the trailing edge strip, and connected to a rotor actuator located in the D spar.

The total bending moment applied to the trailing edge by both tendons is

$$M_{ten} = 2k_{ten}\Delta l_{ten} y_{ten} = \kappa\frac{\Delta l_{ten}}{r_f} = \kappa\delta_f \tag{18}$$

where y_{ten} is tendon mounting offset, $k_{ten}\Delta l_{ten}$ is the force in the tendon, r_f is the spooling pulley radius and $\kappa = 2k_{ten}y_{ten}r_f$ is a constant. Equation (18) shows that the compliant FishBAC camber can be considered as a positive stiffness system, and the required torque is proportional to the rotation angle. Therefore, the dynamic property of the morphing camber can be tailored by using an optimised negative stiffness mechanism. A second pair of tendons are attached to the beam at x_l and couple it to the negative stiffness device, as shown in Fig. 8. So the rear segment can be considered as a two-part system, namely, the length before the mounting point $0 < x < x_l$ and the length after the mounting point $x_l < x < l$.

3.2. Negative stiffness mechanism in a rotating blade system

The chosen negative stiffness mechanism is a spiral pulley negatives stiffness device, as shown in Fig. 9. A linear spring is used to store energy and produce actuating force. As the spiral pulley rotates, its effective diameter changes and the moment arm produced by the profile of the spiral pulley varies. This effect can be tailored to give negative stiffness that counteracts the positive
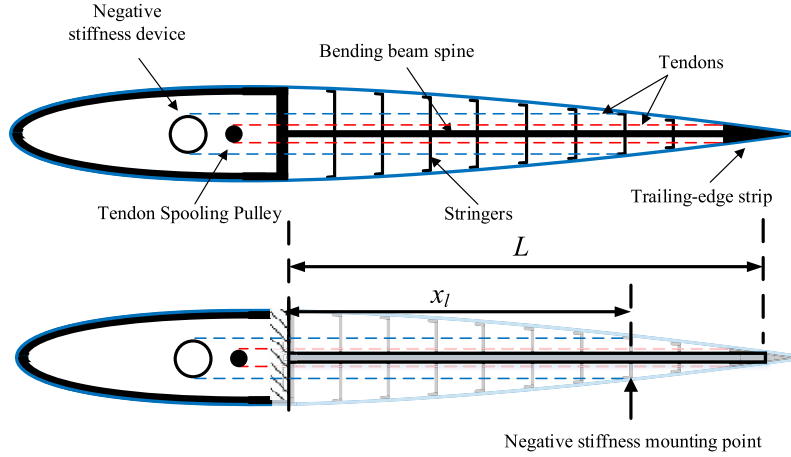
Fig. 8. Schematic representation of a morphing aircraft with assisted negative stiffness design.
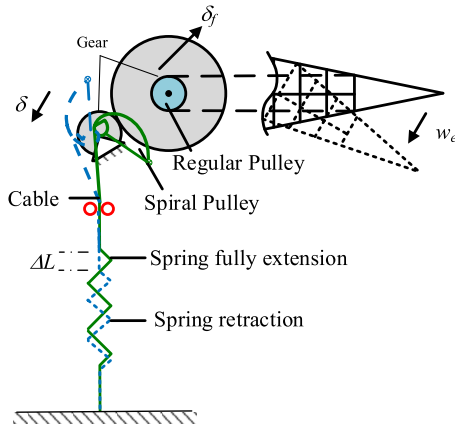

Fig. 9. Schematic of the spiral pulley negative stiffness mechanism for morphing aircraft actuation.

Fig. 10. Schematic of the spiral pulley negative stiffness mechanism for a morphing rotating blade.

stiffness of the actuated structure and is optimised for a given actuation role. It is hard to satisfy both the actuation requirement and the limited space to develop an energy balancing system for large morphing aircraft requirements. Therefore, in order to improve the integrated performance of the total energy balancing system, a gear is proposed as an additional parameter to produce larger tolerances for reducing the dimension of the system. The schematic of the whole system is shown in Fig. 9, from an initial configuration to an actuated configuration.

The spiral pulley is defined as an exponential radius profile in polar coordinates about the centre of rotation

$$r = r_0 + k_1 e^{k_2(\theta + \delta + \delta_0)} \tag{19}$$

where δ is spiral pulley rotation angle and θ is an associated offset angle; δ_0 is the initial pulley rotation angle, and r_0, k_1 and k_2 are parameters of the spiral profile. The spring is designed as an energy storage device with an initial extended length L_0 and K is the spring constant. x_{off} and y_{off} are x-direction and y-direction offsets of the spiral pulley mount.

An extra difficulty occurs because the spiral pulley negative stiffness mechanism is implemented in a rotating blade system, as shown in Fig. 1. The pre-stretched spring locates along the span of the blade and the mass of the spring has an extra centrifugal force, as shown in Fig. 10. When the spring is stretched along the span of the blade, a centrifugal force exists along the spring that reduces the restoring force, which can significantly change the force applied to the spiral pulley. In what follows, the effective stiffness
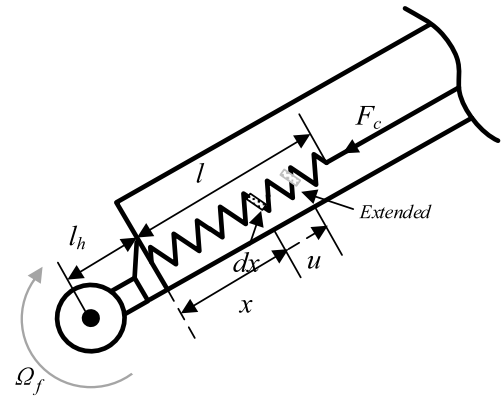
of the spring is investigated by considering the angular speed of the rotating blade.

Fig. 10 shows a spring with a stiffness K that is extended along the span of a blade under the angular speed Ω_f and the centripetal load of spring, F_c. The equation of motion can be obtained as

$$E_s A_s \frac{d^2 u}{dx^2} + \rho_s A_s \Omega_f^2 (l_h + x_s + u_s) = 0 \tag{20}$$

where $\rho_s A_s$ and $E_s A_s$ are the mass unit length and effective axial stiffness of the spring, and l_h is the offset position of the spring. u_s is deformation of spring caused by centrifugal force.

Let

$$\lambda^2 = \frac{\rho_s A_s \Omega_f^2}{EA} = \frac{\rho_s A_s \Omega_f^2}{k_0 l_s} \tag{21}$$

where $K = E_s A_s / l_s$ and l_s is the initial length of the spring. Then

$$\frac{d^2 u_s}{dx_s^2} + \lambda^2 (l_h + x_s + u_s) = 0 \tag{22}$$

Thus, the general solution for the deformation of spring u caused by centrifugal force is

$$u_s = -(l_h + x_s) + A_0 \sin \lambda x_s + B_0 \cos \lambda x_s \tag{23}$$

Using the boundary conditions $u_s(x_s = 0) = 0$ and $u_s(x_s = l_s) = u_l$, the constants in Eq. (23) can be obtained as

Table 1
Initial stiffnesses of the chosen springs.

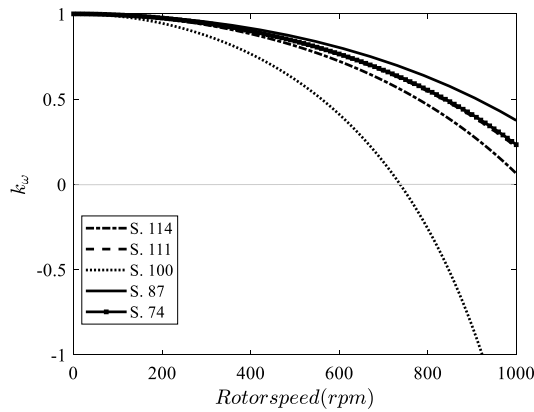| Part Number ((Ashfield Spring Ltd)	S.74	S.87	S.100	S.111	S.114
Stiffness (N/m)	770	920	1060	2000	3090
Estimated Mass per Unit Length (kg/m)	0.3911	0.6582	0.8630	1.2954	1.5399

Fig. 11. Equivalent stiffness of the chosen springs under rotation (legend indicates the part number of the spring).

$$A_0 = \frac{1}{\sin \lambda l_s} \left[u_l + l_h + l_s - l_h \cos \lambda l_s \right], B_0 = l_h \quad (24)$$

We are interested in the force at $x_s = l_s$, which is

$$T_{x_s=l_s} = EA \left. \frac{du_s}{dx_s} \right|_{x_s=l_s} = Kl \left. \frac{du_s}{dx_s} \right|_{x_s=l_s}$$
$$= Kl_s \{-1 + A_0 \lambda \cos \lambda l_s - B_0 \lambda \sin \lambda l_s\} \quad (25)$$

Two interesting features of Eq. (25) are now highlighted. For $\lambda = 0$ (i.e. no rotation) then $T_{x=l} = Ku_l$ as expected. Extracting the term linear in u_l shows that the total stiffness is $K \frac{\lambda l_s}{\tan \lambda x_s}$ and so the reduction in stiffness due to the rotation is $K \left\{1 - \frac{\lambda l_s}{\tan \lambda l_s}\right\}$, which is approximately $\frac{1}{3}K (\lambda l_s)^2$ for small λl_s. The ratio of equivalent stiffness k_ω to static stiffness K can be expressed as

$$k_\omega = \frac{K - K \frac{\lambda l_s}{\tan \lambda l_s}}{K} = 1 - \frac{\lambda l_s}{\tan \lambda l_s} \quad (26)$$

Based on the analysis of equivalent stiffness, some commercially available springs have been investigated with an identical pre-stretch length of 50 mm. The initial stiffness and part number of the chosen springs from Ashfield Spring Ltd are listed in Table 1, the stiffnesses range from 700 to over 3000 N/m and the offset length $l_h = 0$.

Fig. 11 shows how the equivalent stiffness changes with increasing rotation speed. The equivalent stiffness decreases with increasing angular speed, and so a higher initial stiffness must be chosen to design a spiral pulley negative stiffness mechanism for a morphing blade.

In order to show that different negative stiffness characteristics can be designed for the spiral pulley mechanism, three cases are investigated for dynamic tailoring of morphing camber, quasistatic passive energy balancing (case 1), linear stiffness tailoring (case 2) and nonlinear stiffness tailoring (case 3). For a positive stiffness active system, the extra negative stiffness mechanism will effectively reduce actuation effort by using stored energy to achieve passive energy balancing. The quasistatic passive energy balancing means these two systems will be combined together so that they can cancel each other to produce a near-zero stiffness system when the system is actuated in a quasistatic condition. The linear stiffness

Table 2
Parameters for the negative stiffness mechanisms.

Parameter	Case 1	Case 2	Case 3	Units
Initial radius, r_0	−0.0224	−0.0151	−0.0187	m
Pre-exponent term, k_1	0.0154	0.0088	0.0054	–
Exponent term, k_2	0.2135	0.2518	0.5251	–
Initial pulley rotation angle δ_0	−12pi/180	−3pi/180	6pi/180	rad
Drive spring extension, L_0	0.3254	0.2062	0.1582	m
Drive spring rate, K	766.1927	766.2995	766.2895	N/m
Gear ratio, G	4.3309	4.2294	3.7029	–
x_{off}	−0.0005	0.0030	−0.0003	m
y_{off}	0.0268	0.0227	0.0133	m

tailoring means the extra negative stiffness mechanism will effectively cancel part of a positive stiffness active system to produce a reduced stiffness system. This is valuable for morphing structures where the structures support significant loads during frequent actuation. The linear stiffness tailoring used here means the positive stiffness is cut in half as an example. A further improvement is nonlinear stiffness tailoring which adds nonlinearity to the linear stiffness tailoring to produce a nonlinear hardening resonance. The spiral pulley negative stiffness mechanism has been used to provide a satisfactory result for quasistatic passive energy balancing, as shown in Fig. 12(a) [38]. It can be seen that the torque provided by the spiral pulley negative mechanism matches the torque required closely, and the maximum torque required by the additional actuator is less than 2.5 Nm. The performance predicted for the optimised spiral pulley profile is satisfactory and matches the linearised torque requirements well.

The proposed spiral pulley negative stiffness mechanism is then extended to provide a target linear stiffness of the system, which results in an effective reduced stiffness design of morphing camber, as shown in Fig. 12(b). It can be seen that the tailored torque curve (solid) matches the target curve (dash) closely, which provides an effective reduced stiffness of the combined system. Finally, nonlinearity is added to the linear stiffness design of morphing camber by using a spiral pulley negative stiffness mechanism for dynamic tailoring. Fig. 12(c) shows that by using the spiral pulley negative stiffness mechanism, an effective hardening nonlinear stiffness can be obtained for the morphing camber. The nonlinear optimiser fmincon in the MATLAB Global Optimization Toolbox was used to optimise the objective function. The resulting parameters of the three cases are shown in Table 2.

Fig. 12 shows that the evolution of torque with rotation for the spring and the FishBAC and the net torque of the whole system. Part (a) shows the 'energy balancing' case described in previous work [38], which does not consider dynamic response, and largely eliminates the structural stiffness of the system. Part (b) indicates the new approach in which the stiffness of the system is not eliminated, but reduced to give a desired resonant frequency to assist dynamic actuation, assuming that a negative linear stiffness term can be applied. Part (c) shows the same, but with the more desirable assumption of an optimised nonlinear stiffness applied via the spiral pulley system.

Based on the investigation of this study, it can be seen that the spiral pulley negative stiffness mechanism provides a significant contribution to tailor the positive stiffness system (i.e. FishBAC). While the optimised parameters of the spiral pulley obtained here are only simulated, they provide insight into different effective stiffnesses of the combined system, both linear and nonlinear. It is
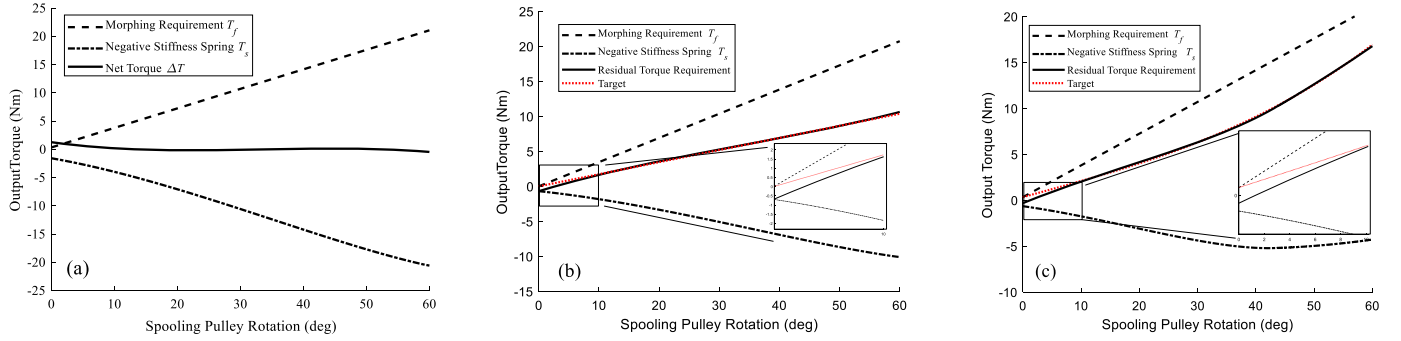
Fig. 12. (a) Passive energy balancing [38]. (b) Linear stiffness tailoring. (c) Nonlinear stiffness tailoring.

shown that the negative stiffness is scalable and highly tailorable to allow for different conditions. Therefore, a further investigation will link the negative spiral pulley system to the morphing aerofoil as a passive energy balancing system to reduce the required load through resonant actuation. The negative spiral pulley system is parameterised by a negative stiffness constant to show how it will influence the dynamic characteristics of the morphing camber system in the following section.

The extended spring is used here to store energy and produce actuating force. As the spiral pulley rotates, its effective diameter changes, and the moment arm produced by the profile of the spiral pulley varies, so that the desired torque could be produced. Therefore, the spring is always in tension in the whole actuation process which means that only part of the initial extension length is released and the spring will be still extended after actuation. In other word, the tensioning force always exists in the negative stiffness system.

This being the cause, issues such as free play can be avoided because the system is always under tension.

4. Resonant passive energy balancing

4.1. Linear resonant passive energy balancing

In order to investigate the resonant passive energy balancing for morphing camber actuation, the FishBAC morphing camber is recalled here for study. Note that in this analysis, no detailed modelling of aerodynamic forces acting on the morphing section is included; it is believed that such effects could be roughly captured through equivalent additions to the structural stiffness and damping and would not affect the overall conclusions of this work, with more sophisticated modelling as the topic of future work. The equation of motion of the morphing segment shown in Fig. 8 has the form

$$EI\frac{\partial^4 w}{\partial x^4} + \rho(x)\left(\frac{\partial^2 w}{\partial t^2}\right) = 0 \tag{27}$$

Therefore, the location of the negative stiffness mechanism mounting point is investigated in order to provide a full range of target frequency. The traditional differential equation of motion has the compatibility conditions at $x = x_l$ as

$$w_1\left(x_l^L, t\right) = w_2\left(x_l^R, t\right), \quad \frac{\partial}{\partial x}w_1\left(x_l^L, t\right) = \frac{\partial}{\partial x}w_2\left(x_l^R, t\right),$$

$$\frac{\partial^3}{\partial x^3}w_1\left(x_l^L, t\right) = \frac{\partial^3}{\partial x^3}w_2\left(x_l^R, t\right), \tag{28a}$$

$$\frac{\partial^2}{\partial x^2}w_1\left(x_l^L, t\right) - \frac{\partial^2}{\partial x^2}w_2\left(x_l^R, t\right) = -\bar{k}\frac{\partial}{\partial x}w_1\left(x_l^L, t\right)$$

where $\bar{k} = k/EI$, and k is a parameterised negative torsional stiffness derived from the spiral pulley negative stiffness mechanism. w_1 and w_2 represent the displacements forward and aft of the tendon connection point, and the superscripts L and R represent the location just to the left or right of x_l.

The other boundary conditions are

$$w_1(0, t) = 0, \quad \frac{\partial}{\partial x}w_1(0, t) = 0, \quad \frac{\partial^2}{\partial x^2}w_2(l, t) = 0, \tag{28b}$$

$$\frac{\partial^3}{\partial x^3}w_2(l, t) = 0$$

The general solution for the displacement w_1 of first subsystem and w_2 of first subsystem can be expressed as

$$w_1(x, t) = \sum_{j=1}^{n}\phi_{1j}\xi_{1j}$$
$$w_2(x, t) = \sum_{j=1}^{n}\phi_{2j}\xi_{2j} \tag{29}$$

where ϕ are the basis functions and ξ are generalised displacements. The general mathematical expressions for ϕ_{1j} and ϕ_{2j} are given by

$$\phi_{1j} = A_{1j}\sin\beta_j x + B_{1j}\cos\beta_j x + C_{1j}\sinh\beta_j x + D_{1j}\cosh\beta_j x$$
$$\phi_{2j} = A_{2j}\sin\beta_j x + B_{2j}\cos\beta_j x + C_{2j}\sinh\beta_j x + D_{2j}\cosh\beta_j x \tag{30}$$

The wave numbers β_j can be found from the roots of the transcendental equation in Appendix A.

Fig. 13 shows the tailored frequency by using different negative stiffnesses $\bar{k}$ and different assisted locations x_l of the morphing camber. Fig. 13(a) shows the first three natural frequencies when $\bar{k} = 30$ and highlights that the 2nd and 3rd modal frequencies vary by less than 1%. Therefore, only the first natural frequency of a camber morphing system has a distinct tailoring and the reduction of the tailored frequency is gradual as the assisted location is changed, which is shown in Fig. 13(b). Therefore, a full range of target frequencies can be tailored by using the negative stiffness mechanism at the selected connection location.

Now, a detailed case by using the negative stiffness for an actuated morphing camber model under a bending moment is considered. The schematic of the actuated morphing camber model can be seen in Fig. 7 as well as the total bending moment applied to the trailing edge. As the moment is applied at a single point on the trailing edge strip, the traditional equation of motion of the morphing segment has the form

$$EI\frac{\partial^4 w}{\partial x^4} + c\frac{\partial w}{\partial t} + \rho(x)\left(\frac{\partial^2 w}{\partial t^2}\right) = -M_{ten}\frac{d}{dx}\delta(x - x_l) \tag{31}$$
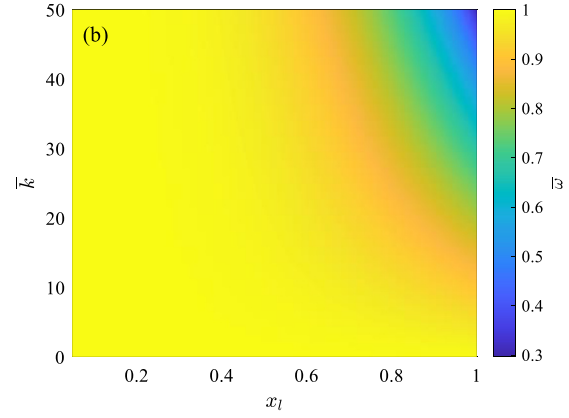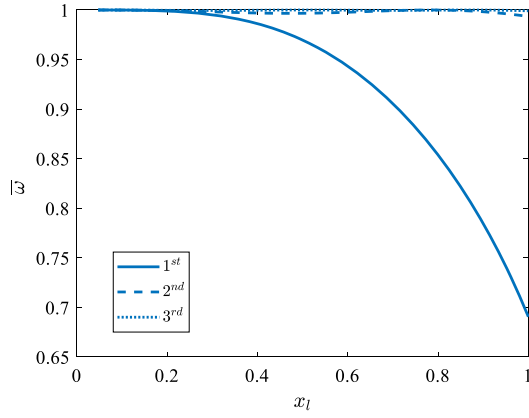
Fig. 13. Results of the assisted negative stiffness design (different negative linear terms and different assisted locations), $\overline{\omega}$ is the ratio of PEB assisted and unassisted natural frequencies. (a) $\overline{k} = 30$. (b) First tailored frequency.
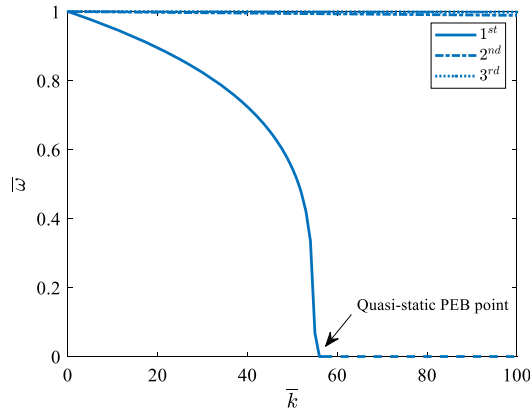

Fig. 14. Results of the assisted negative stiffness design at the tip of morphing camber. $\overline{\omega}$ is the frequency ratio (PEB assisted)/unassisted.

where δ is the Dirac delta function.

Meanwhile, it is assumed that the negative stiffness is mounted at the tip coincident with the location of the actuation moment, i.e. $x_l = L$, and the boundary conditions can be summarised as

$$w(0,t) = 0, \quad w'(0,t) = 0, \quad EIw'''(x_l, t) = 0,$$
$$w''(x_l, t) = -\overline{k}w'(x_l, t) \tag{32}$$

where the prime indicates the derivative with respect to position x, $\rho(x)$ is the linear density and $\overline{k} = k/EI$, where k is a parameterised negative torsional stiffness derived from the spiral pulley negative stiffness mechanism.

The natural frequency of the morphing camber model can be solved by dropping the moment term and using the basis functions $\phi_1, \phi_2, \ldots \phi_j$ and generalised displacements $\xi_1, \xi_2, \ldots \xi_j$ (Appendix B). The wave numbers β_j in the basis functions can be found from the roots of the following transcendental equation:

$$\overline{k} = \beta_j \frac{1 + \cos\beta_j L \cosh\beta_j L}{\cos\beta_j L \sinh\beta_j L + \cosh\beta_j L \sin\beta_j L}. \tag{33}$$

Fig. 14 shows that a linear negative stiffness mechanism provides a significant contribution to reduce the first natural frequency of a camber morphing system, but has little influence on the higher modes. Moreover, the tailored frequency reduces gradually for smaller $\overline{k}$ and then the sensitivity becomes much larger. It's worth noting that if the natural frequency is very sensitive to variations in the stiffness, the target frequency is cannot be too small. In addition, the quasi-static PEB occurs when $\overline{\omega} = 0$, where

in principle no energy is required to move the system, other than to overcome dissipation and inertia [36,37]. For larger negative spring stiffnesses, i.e. beyond the quasi-static PEB point, the system is unstable.

Based on the results shown in Fig. 14, the morphing camber is considered to generate resonance actuation by using a negative stiffness mechanism under a bending moment excitation. It is assumed that the morphing segment is excited by a harmonic moment $M(t)$ of amplitude M_0 and frequency ω_f. Therefore, Eq. (32) becomes, in model coordinates,

$$\ddot{\xi}_j(t) + 2\zeta_j\omega_j\dot{\xi}_j(t) + \omega_j^2\xi_j(t) = M(t)\phi_j'(x_l) \tag{34}$$

where $\zeta_j = c/2\omega_j$.

The steady solution of Eq. (34) is

$$\xi_j(t) = B\alpha\sin(\omega_f t + \theta) \tag{35}$$

where $B = M(t)\phi_j'(x_1)/\omega_j^2$, $\alpha = 1/\sqrt{\left(1-\overline{\omega}_j^2\right)^2 + \left(2\xi_j\overline{\omega}_j\right)^2}$, $\theta = \tan^{-1}\left(2\xi_j\overline{\omega}_j/\left(1-\overline{\omega}_j^2\right)\right)$ and $\overline{\omega}_j = \omega_f/\omega_j$.

The energy dissipated by damping for the steady solution Eq. (35) becomes

$$W_d = \int_0^T 2\zeta_j\omega_j\left(\dot{\xi}_j(t)\right)^2 dt$$
$$= \int_0^{2\pi/\omega_f} (B\alpha)^2 2\zeta_j\omega_j\omega_f^2\cos^2(\omega_f t + \theta) dt$$
$$= 2\pi(B\alpha)^2\zeta_j\omega_j\omega_f \tag{36}$$

where W_d is the energy dissipated by the damper. By considering the instantaneous power exerted by the actuator to the structure discussed in Eq. (5), so the input energy W_+ from the actuator over one cycle of actuation can be given by Eq. (8) as

$$W_+ = \int_0^T p_+ dt$$
$$= \int_0^{2\pi/\omega_f} \left|\left(M_0\phi_j'(x_l)\right)\omega_f B\alpha\sin\omega_f t\cos(\omega_f t + \theta)\right| dt$$
$$= \frac{1}{2}\left(M_0\phi_j'(x_l)\right)\omega_f B\alpha\left(\sin\theta\frac{\pi+2\theta}{\omega_f} + 2\frac{1}{\omega_f}\cos\theta\right) \tag{37}$$
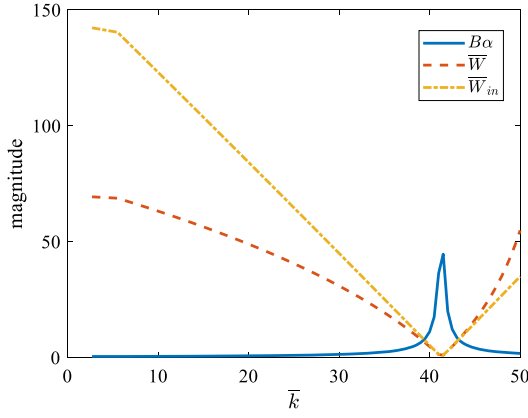
Fig. 15. Results of an assisted negative stiffness design for different negative linear terms. $\overline{W} = W_+/W_d$ and $\overline{W}_{in} = W_+/\min W_+$.

Fig. 15 shows an example case under actuation at half of its unassisted first natural frequency and three indices have been shown, namely $B\alpha$, $\overline{W}$ and $\overline{W}_{in}$. $B\alpha$ is the amplitude of the steady solution shown in Eq. (35), which is used to evaluate the output under the same actuation. $\overline{W}$ represents the mean energy dissipated, that is ratio between the input and dissipated energies, which is used to evaluate the reduction in the required work for a constant required output. $\overline{W}_{in}$ is the normalised W_+, given by the ratio between the required input energy and the minimum energy, $\min W_+$, that is dissipated by the damper. In order to generate resonant actuation, a PEB is used to assist the actuation at the frequency $\Omega_0 = \omega_n/2$, i.e. when $\overline{k} = 42$. It can be seen that a larger output $B\alpha$ can be obtained if the same actuation is applied. Furthermore, the resonant actuation requires minimum work to assume a constant required output, which is shown by $\overline{W}$ and W_+. Thus $\min W_+$ is equal to W_d at resonance, which supports the discussion in Section 2 that the performance of the system is limited by the system damping.

4.2. Resonant passive energy balancing with nonlinearity

Fig. 14 shows that the negative stiffness mounting point is best located near the tip of a morphing camber, which can provide a reliable means to tailor the target frequency, if this frequency is not too small. However, through the results of Section 2, it is known that at a nonlinear resonance, the amplitude is limited by both the nonlinearity and the damping, giving a response that is more robust in the presence of damping and forcing uncertainties than a linear resonant response. Therefore, nonlinearity will be introduced into the negative stiffness element. Here, a cubic term is added and expressed as

$$EI \sum_{j=1}^{\infty} \phi_j''(x_l) \xi_j = -k \sum_{j=1}^{\infty} \phi_j'(x_l) \xi_j + k_n \left(\sum_{j=1}^{\infty} \phi_j'(x_l) \xi_j \right)^3 \quad (38)$$

where $x_l = L$. Equation (38) presents a modified boundary condition from Eq. (32), considering the nonlinearity. In order to investigate the dynamic response of a nonlinear negative stiffness assisted morphing blade, Eq. (34) and the boundary conditions, Eq. (38), can be approximated by assuming that $\xi_j(t) = Q_j \sin(\omega_f t + \theta_j)$. Thus, using the harmonic balance method (HBM) [43], gives

$$\begin{cases} R_1 := \left(\omega_j^2 - \omega_f^2\right) Q_j \sin\theta_j - 2\zeta_j\omega_j\omega_f Q_j \cos\theta_j \\ \qquad -M_0\phi_j'(x_1)/m_j = 0 \\ R_2 := \left(\omega_j^2 - \omega_f^2\right) Q_j \cos\theta_j + 2\xi_j\omega_j\omega_f Q_j \sin\theta_j = 0 \\ R_3 := \phi_j''(x_l) + \overline{k}\phi_j'(x_l) - \frac{3}{4}\overline{k}_n \left(\phi_j'(x_l)\right)^3 Q_j^2 = 0 \end{cases} \quad (39)$$

where Q_j, θ_j and ω_j are unknowns. R_1 and R_2 are two algebraic equations derived from the harmonics to solve two unknowns Q_j and θ_j. R_3 is a supplementary equation from boundary condition, i.e. Eq. (38), and this equation is coupled with the unknowns Q_j, so that the unknown ω_j may be calculated to ensure resonance by solving the simultaneous equations.

Solving Eq. (39) yields

$$\begin{cases} \left(\left(\omega_j^2 - \omega_f^2\right) Q_j\right)^2 + \left(2\zeta_j\omega_j\omega_f Q_j\right)^2 = \left(M_0\phi_j'(x_1)/m_j\right)^2 \\ \cos\theta_j = \frac{2\zeta_j\omega_j\omega_f Q_j}{-M_0\phi_j'(x_1)/m_j}, \sin\theta_j = \frac{\left(\omega_j^2-\omega_f^2\right)Q_j}{M_0\phi_j'(x_1)/m_j} \\ \phi_j''(x_l) + \overline{k}\phi_j'(x_l) - \frac{3}{4}\overline{k}_n \left(\phi_j'(x_l)\right)^3 Q_j^2 = 0 \end{cases} \quad (40)$$

where Q_j is the amplitude and θ_j is the phase of the response. Solving Eq. (40) for ω_f gives the frequency amplitude relationship as

$$\omega_f^2 = \left(\omega_j^2 + \frac{(2\zeta_j\omega_j)^2}{2}\right)$$

$$\pm \left(-\omega_j^2(2\zeta_j\omega_j)^2 + \frac{(2\zeta_j\omega_j)^4}{4} + \frac{\left(M_0\phi_j'(x_1)/m_j\right)^2}{Q_j^2}\right)^{\frac{1}{2}} \quad (41)$$

where Eq. (41) gives the response of the system in the region where multiple stable solutions may exist.

Fig. 16 shows the frequency-response curve for different values of actuation amplitude M_0, for both the linear and nonlinear systems. A linear resonant system can provide the largest amplitude, and the nonlinearity $\overline{k}_n$ reduces the amplitude and makes the system harden. However, the existence of the nonlinearity can give a response that is more robust in the presence of damping and forcing uncertainties than a linear resonant response. The target amplitude $Q = 0.15$ is actuated by an assumed actuation amplitude $M_0 = 0.5$ at a desired actuation frequency. Fig. 16(b) shows that when the actuation is changed, the resonant system gives a relatively small change in output amplitude with nonlinearity compared with the doubling of output amplitude from the linear system shown in Fig. 16(a). Namely, the variability of response (grey dashed line) is smaller if nonlinearity is introduced in a resonant actuation system. When the actuation amplitude changes from 0.4 to 1, the variation of the output amplitude is 0.12 to 0.3 in the linear resonant system but only 0.12 to 0.18 in the nonlinear resonant system. Therefore, the selected nonlinearity in the negative stiffness mechanism used to generate resonant actuation can reduce the required actuation and stabilise the system.

Moreover, Fig. 16 shows the results of a morphing blade with a PEB optimised for actuation at frequency $\omega_f = \omega_n/2$, i.e. rotor frequency. Meanwhile, the morphing will be operated at one cycle per revolution, which means the actuator frequency is equal to the rotor frequency. Therefore, the natural frequency of the blade is tailored by the negative stiffness mechanism to give the actuation frequency for resonance.

This example shows that nonlinearity can help to stabilise the system even if the actuation power fluctuates. Therefore, although
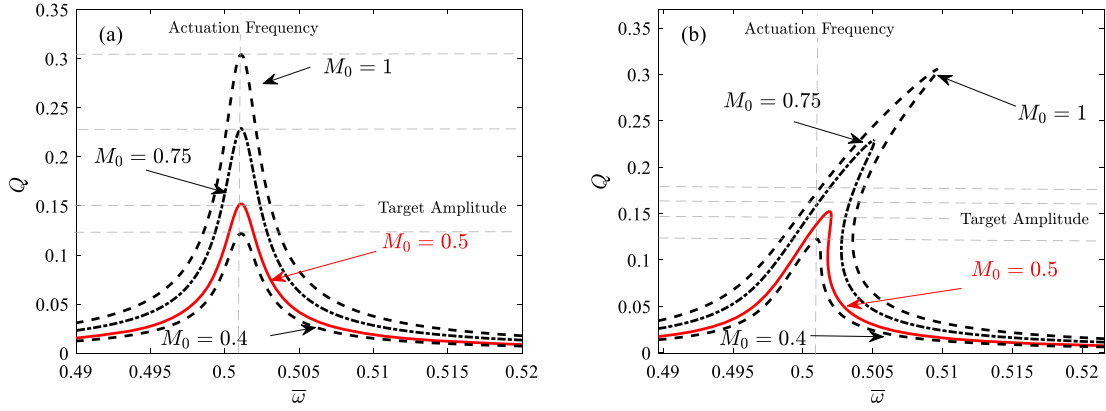
Fig. 16. Frequency response. (a) linear negative stiffness (b) nonlinear negative stiffness $\bar{k}_n/\bar{k} = 0.1$.

a quasi-static PEB system with a zero stiffness characteristic can be easily influenced by small disturbances, adding nonlinearity can avoid such a problem. Hence, the negative stiffness mechanism can be optimised by considering the nonlinearity required to generate a desired amplitude.

5. Conclusion

A new concept to generate resonant passive energy balancing for a morphing blade has been presented. The novelty of this concept is to reduce the natural frequency of a structure to a desired actuation frequency by using a designed negative stiffness. A spiral pulley system has been proposed as the negative stiffness mechanism to achieve linear frequency tailoring and nonlinear frequency tailoring. The equivalent stiffness of the extended spring used in the negative stiffness mechanism has been investigated by considering the centrifugal force. The dynamic characteristics of a forced system using an additional negative stiffness element are studied, which shows that the actuation power requirement can be reduced. In particular, the presence of the negative stiffness has been shown to cause effects such as a reduced natural frequency and an amplitude dependent natural frequency. The mechanism has been considered to provide a linear negative stiffness property, which is then extended to include nonlinearity, which can restrict the resonance amplitude. Exploiting such a negative stiffness concept is of significant interest in the wide field of energy and power reduction applications.

Declaration of competing interest

The authors declare that they have no known competing financial interests or personal relationships that could have appeared to influence the work reported in this paper.

Acknowledgement

Appendix A

The general solution for the displacement w_1 of first subsystem and w_2 of first subsystem can be expressed as

$$w_1(x,t) = \sum_{j=1}^{n} \phi_{1j} \xi_{1j}$$
$$w_2(x,t) = \sum_{j=1}^{n} \phi_{2j} \xi_{2j}$$
(A.1)

The mathematical expression ϕ_{1j} and ϕ_{2j} of are given by

$$\phi_{1j} = A_{1j} \sin\beta_j x + B_{1j} \cos\beta_j x + C_{1j} \sinh\beta_j x + D_{1j} \cosh\beta_j x$$
$$\phi_{2j} = A_{2j} \sin\beta_j x + B_{2j} \cos\beta_j x + C_{2j} \sinh\beta_j x + D_{2j} \cosh\beta_j x$$
(A.2)

Inserting Eqs. (A.2) into compatibility conditions yields

$$\begin{bmatrix} A_{2j} \\ B_{2j} \\ C_{2j} \\ D_{2j} \end{bmatrix} = \begin{bmatrix} u_{11}^j & u_{12}^j & u_{13}^j & u_{14}^j \\ u_{21}^j & u_{22}^j & u_{23}^j & u_{24}^j \\ u_{31}^j & u_{32}^j & u_{33}^j & u_{34}^j \\ u_{41}^j & u_{42}^j & u_{43}^j & u_{44}^j \end{bmatrix} \begin{bmatrix} A_{1j} \\ B_{1j} \\ C_{1j} \\ D_{1j} \end{bmatrix}$$
$$= U_{4\times4} \times \begin{bmatrix} A_{1j} \\ B_{1j} \\ C_{1j} \\ D_{1j} \end{bmatrix}$$
(A.3)

where

$$\begin{bmatrix} u_{11}^j & u_{12}^j & u_{13}^j & u_{14}^j \\ u_{21}^j & u_{22}^j & u_{23}^j & u_{24}^j \\ u_{31}^j & u_{32}^j & u_{33}^j & u_{34}^j \\ u_{41}^j & u_{42}^j & u_{43}^j & u_{44}^j \end{bmatrix}$$
$$= \begin{bmatrix} 0 & \sin(\beta_j x_l) - \frac{k\cos(\beta_j x_l)}{2EI\beta_j} & -\cos(\beta_j x_l) & \frac{k\cos(\beta_j x_l)}{2EI\beta_j} \\ 0 & \cos(\beta_j x_l) + \frac{k\sin(x_l\beta_j)}{2EI\beta_j} & \sin(\beta_j x_l) & -\frac{k\sin(\beta_j x_l)}{2EI\beta_j} \\ -\cosh(\beta_j x_l) & -\frac{k\cosh(\beta_j x_l)}{2EI\beta_j} & 0 & \sinh(\beta_j x_l) + \frac{k\cosh(\beta_j x_l)}{2EI\beta_j} \\ -\sinh(\beta_j x_l) & -\frac{k\sinh(\beta_j x_l)}{2EI\beta_j} & 0 & \cosh(\beta_j x_l) + \frac{k\sinh(\beta_j x_l)}{2EI\beta_j} \end{bmatrix}^T$$

Then, the boundary conditions at $x = 0$ yield

$$B_{1j} + D_{1j} = 0, \qquad A_{1j} + C_{1j} = 0$$
(A.4a)

The boundary conditions at $x = x_l$ yield

$$T_{2\times4} \times \begin{bmatrix} A_{2j} \\ B_{2j} \\ C_{2j} \\ D_{2j} \end{bmatrix} = \begin{bmatrix} 0 \\ 0 \end{bmatrix}$$
(A.4b)

where

$T_{2\times4} =$

$$\begin{bmatrix} -\cos\left((l-x_l)\beta_j\right) & -\sin\left((l-x_l)\beta_j\right) & \cosh\left((l-x_l)\beta_j\right) & \sinh\left((l-x_l)\beta_j\right) \\ \sin\left((l-x_l)\beta_j\right) & -\cos\left((l-x_l)\beta_j\right) & \sinh\left((l-x_l)\beta_j\right) & \cosh\left((l-x_l)\beta_j\right) \end{bmatrix}$$

Then, the Eq. (A.4b) can be rewritten by applying Eq. (A.3)

$$T_{2\times4} \times \begin{bmatrix} A_{2j} \\ B_{2j} \\ C_{2j} \\ D_{2j} \end{bmatrix} = T_{2\times4} \times U_{4\times4} \times \begin{bmatrix} A_{1j} \\ B_{1j} \\ C_{1j} \\ D_{1j} \end{bmatrix} = r_{2\times4} \times \begin{bmatrix} A_{1j} \\ B_{1j} \\ C_{1j} \\ D_{1j} \end{bmatrix}$$

$$= \begin{bmatrix} 0 \\ 0 \end{bmatrix} \tag{A.5}$$

where

$$r_{2\times4} = \begin{bmatrix} r_{11} & r_{12} & r_{13} & r_{14} \\ r_{21} & r_{22} & r_{23} & r_{24} \end{bmatrix}$$

Then, from Eq. (A.4a), it can be finally obtained as

$$\begin{bmatrix} r_{11} - r_{13} & r_{12} - r_{14} \\ r_{21} - r_{23} & r_{22} - r_{24} \end{bmatrix} \begin{bmatrix} A_{1j} \\ B_{1j} \end{bmatrix} = \begin{bmatrix} 0 \\ 0 \end{bmatrix} \tag{A.6}$$

The requirement for non-trivial solutions for A_1 and B_1 in Eqs. (A.6) produces the characteristic determinant equation for the maximum fundamental frequency parameter as

$$\det \begin{bmatrix} r_{11} - r_{13} & r_{12} - r_{14} \\ r_{21} - r_{23} & r_{22} - r_{24} \end{bmatrix} = 0 \tag{A.7}$$

Appendix B

The deformation w is expressed as

$$w(x,t) = \phi_1 \xi_1 + \phi_2 \xi_2 + \cdots = \sum_{j=1}^{n} \phi_j \xi_j \tag{B.1}$$

where $\phi_1, \phi_2, \ldots \phi_j$ are the basis functions and $\xi_1, \xi_2, \ldots \xi_j$, are generalised displacements. The mathematical expression ϕ_j is given by

$$\phi_j = A_j \sin\beta_j x + B_j \cos\beta_j x + C_j \sinh\beta_j x + D_j \cosh\beta_j x \tag{B.2}$$

The frequency can be shown as,

$$\omega_j = \beta_j^2 \sqrt{\frac{EI}{m}} \tag{B.3}$$

where $m = \int_0^l \phi_j \rho(x) \phi_j^T dx = 1$, the boundary conditions at $x = 0$ yield

$$B_j + D_j = 0, \quad A_j + C_j = 0 \tag{B.4}$$

Recall Eq. (B.2) with ignore high order Eq. (B.1) can be expressed as

$$\phi_j''(x_l) = -\bar{k}\phi_j'(x_l) \tag{B.5}$$

where $\bar{k} = k/EI$, k is torsional stiffness. Then, the final condition is

$$EI\beta_j^2 \left[A_j \left(\sin\beta_j l + \sinh\beta_j l \right) + B_j \left(\cos\beta_j l + \cosh\beta_j l \right) \right]$$
$$= k\beta_j \left[A_j \left(-\cos\beta_j l + \cosh\beta_j l \right) + B_j \left(\sin\beta_j l + \sinh\beta_j l \right) \right] \tag{B.6}$$

Finally, the wave numbers β_j can be found from the roots of the following transcendental equation:

$$\bar{k} = \beta_j \frac{1 + \cos\beta_j l \cosh\beta_j l}{\cos\beta_j l \sinh\beta_j l + \cosh\beta_j l \sin\beta_j l}. \tag{B.7}$$

References

[1] S. Barbarino, O. Bilgen, R.M. Ajaj, M.I. Friswell, D.J. Inman, A review of morphing aircraft, J. Intell. Mater. Syst. Struct. 22 (2011) 823–877, https://doi.org/10.1177/1045389X11414084.

[2] R.M. Ajaj, C.S. Beaverstock, M.I. Friswell, Morphing aircraft: the need for a new design philosophy, Aerosp. Sci. Technol. (2016), https://doi.org/10.1016/j.ast.2015.11.039.

[3] P. Santos, J. Sousa, P. Gamboa, Variable-span wing development for improved flight performance, J. Intell. Mater. Syst. Struct. 28 (2017) 961–978, https://doi.org/10.1177/1045389X15595719.

[4] M.T.S. Alves, V. Steffen, M. Castro dos Santos, M.A. Savi, S. Enemark, I.F. Santos, Vibration control of a flexible rotor suspended by shape memory alloy wires, J. Intell. Mater. Syst. Struct. 29 (2018) 2309–2323, https://doi.org/10.1177/1045389X18758179.

[5] C.S. Beaverstock, J. Fincham, M.I. Friswell, R.M. Ajaj, R. De Breuker, N. Werter, Effect of symmetric & asymmetric span morphing on flight dynamics, in: AIAA Atmos. Flight Mech. Conf., American Institute of Aeronautics and Astronautics, Reston, Virginia, 2014.

[6] H. Namgoong, W.A. Crossley, A.S. Lyrintzis, Aerodynamic optimization of a morphing airfoil using energy as an objective, AIAA J. 45 (2007) 2113–2124, https://doi.org/10.2514/1.24355.

[7] A. Paternoster, R. Loendersloot, A. de, R. Akkerm, Smart actuation for helicopter rotorblades, in: Smart Actuation Sens. Syst. - Recent Adv. Futur. Challenges, 2012.

[8] B. Yan, P. Dai, R. Liu, M. Xing, S. Liu, Adaptive super-twisting sliding mode control of variable sweep morphing aircraft, Aerosp. Sci. Technol. 92 (2019) 198–210, https://doi.org/10.1016/j.ast.2019.05.063.

[9] J. Zhang, A.D. Shaw, C. Wang, H. Gu, M. Amoozgar, M.I. Friswell, B.K.S. Woods, Aeroelastic model and analysis of an active camber morphing wing, Aerosp. Sci. Technol. 111 (2021) 106534, https://doi.org/10.1016/j.ast.2021.106534.

[10] J.P. Eguea, G. Pereira Gouveia da Silva, F. Martini Catalano, Fuel efficiency improvement on a business jet using a camber morphing winglet concept, Aerosp. Sci. Technol. 96 (2020) 105542, https://doi.org/10.1016/j.ast.2019.105542.

[11] H. Yeo, Design and aeromechanics investigation of compound helicopters, Aerosp. Sci. Technol. 88 (2019) 158–173, https://doi.org/10.1016/j.ast.2019.03.010.

[12] F. Cardito, R. Gori, J. Serafini, G. Bernardini, M. Gennaretti, Space-time accurate finite-state dynamic inflow modeling for aeromechanics of rotorcraft, Aerosp. Sci. Technol. 95 (2019) 105454, https://doi.org/10.1016/j.ast.2019.105454.

[13] P. Moser, S. Barbarino, F. Gandhi, Helicopter rotor-blade chord extension morphing using a centrifugally actuated Von Mises truss, J. Aircr. 51 (2014) 1422–1431, https://doi.org/10.2514/1.C032299.

[14] S.R. Hall, E.F. Prechtl, Development of a piezoelectric servoflap for helicopter rotor control, Smart Mater. Struct. 5 (1996) 26–34, https://doi.org/10.1088/0964-1726/5/1/004.

[15] R. Mallick, R. Ganguli, M.S. Bhat, An experimental and numerical study of piezoceramic actuator hysteresis in helicopter active vibration control, Proc. Inst. Mech. Eng., G J. Aerosp. Eng. 228 (2014) 690–705, https://doi.org/10.1177/0954410013478254.

[16] J. Rauleder, B.G. Van Der Wall, A. Abdelmoula, D. Komp, S. Kumar, V. Ondra, B. Titurus, B.K.S. Woods, Aerodynamic performance of morphing blades and rotor systems, in: Annu. Forum Proc. - AHS Int., 2016.

[17] G.Q. Zhao, Q.J. Zhao, Dynamic stall control on rotor airfoil via combination of synthetic jet and droop leading-edge, in: Annu. Forum Proc. - AHS Int., 2015.

[18] G. Zhao, Q. Zhao, Dynamic stall control optimization of rotor airfoil via variable droop leading-edge, Aerosp. Sci. Technol. 43 (2015) 406–414, https://doi.org/10.1016/j.ast.2015.03.022.

[19] S. Barbarino, F. Gandhi, S.D. Webster, Design of extendable chord sections for morphing helicopter rotor blades, J. Intell. Mater. Syst. Struct. 22 (2011) 891–905, https://doi.org/10.1177/1045389X11414077.

[20] F. Gandhi, M. Frecker, A. Nissly, Design optimization of a controllable camber rotor airfoil, AIAA J. 46 (2008) 142–153, https://doi.org/10.2514/1.24476.

[21] B.K. Woods, O. Bilgen, M.I. Friswell, Wind tunnel testing of the fish bone active camber morphing concept, J. Intell. Mater. Syst. Struct. 25 (2014) 772–785, https://doi.org/10.1177/1045389X14521700.

[22] Sang Joon Shin, C.E.S. Cesnik, W.K. Wilkie, M.L. Wilbur, Design and manufacturing of a model-scale active twist rotor prototype blade, J. Intell. Mater. Syst. Struct. 19 (2008) 1443–1456, https://doi.org/10.1177/1045389X07088051.

[23] D. Thakkar, R. Ganguli, Induced shear actuation of helicopter rotor blade for active twist control, Thin-Walled Struct. 45 (2007) 111–121, https://doi.org/10.1016/j.tws.2006.11.001.

[24] M.R. Amoozgar, A.D. Shaw, J. Zhang, M.I. Friswell, Composite blade twist modification by using a moving mass and stiffness tailoring, AIAA J. 57 (2019) 4218–4225, https://doi.org/10.2514/1.J057591.

[25] I. Dimino, G. Amendola, B. Di Giampaolo, G. Iannaccone, A. Lerro, Preliminary design of an actuation system for a morphing winglet, in: 2017 8th Int. Conf. Mech. Aerosp. Eng. ICMAE 2017, 2017, pp. 416–422.

[26] A. Kakogawa, S. Jeon, S. Ma, Stiffness design of a resonance-based planar snake robot with parallel elastic actuators, IEEE Robot. Autom. Lett. 3 (2018) 1284–1291, https://doi.org/10.1109/LRA.2018.2797261.

[27] J.-S. Kim, K.W. Wang, E.C. Smith, Development of a resonant trailing-edge flap actuation system for helicopter rotor vibration control, Smart Mater. Struct. 16 (2007) 2275–2285, https://doi.org/10.1088/0964-1726/16/6/030.

[28] J.-S. Kim, K.W. Wang, E.C. Smith, Synthesis and control of piezoelectric resonant actuation systems with buckling-beam motion amplifier, AIAA J. 46 (2008) 787–791, https://doi.org/10.2514/1.32216.

[29] O. Bilgen, A.F. Arrieta, M.I. Friswell, P. Hagedorn, Dynamic control of a bistable wing under aerodynamic loading, Smart Mater. Struct. 22 (2013) 025020, https://doi.org/10.1088/0964-1726/22/2/025020.

[30] A.F. Arrieta, O. Bilgen, M.I. Friswell, P. Hagedorn, Dynamic control for morphing of bi-stable composites, J. Intell. Mater. Syst. Struct. 24 (2013) 266–273, https://doi.org/10.1177/1045389X12449918.

[31] C.T. Bolsman, J.F.L. Goosen, F. van Keulen, Design overview of a resonant wing actuation mechanism for application in flapping wing MAVs, Int. J. Micro Air Veh. 1 (2009) 263–272, https://doi.org/10.1260/175682909790291500.

[32] B.K.S. Woods, I. Dayyani, M.I. Friswell, Fluid/structure-interaction analysis of the fish-bone-active-camber morphing concept, J. Aircr. 52 (2015) 307–319, https://doi.org/10.2514/1.C032725.

[33] J.H.S. Fincham, M.I. Friswell, Aerodynamic optimisation of a camber morphing aerofoil, Aerosp. Sci. Technol. 43 (2015) 245–255, https://doi.org/10.1016/j.ast.2015.02.023.

[34] S. Murugan, B.K.S. Woods, M.I. Friswell, Hierarchical modeling and optimization of camber morphing airfoil, Aerosp. Sci. Technol. 42 (2015) 31–38, https://doi.org/10.1016/j.ast.2014.10.019.

[35] B.K.S. Woods, L. Parsons, A.B. Coles, J.H.S. Fincham, M.I. Friswell, Morphing elastically lofted transition for active camber control surfaces, Aerosp. Sci. Technol. 55 (2016) 439–448, https://doi.org/10.1016/j.ast.2016.06.017.

[36] J. Zhang, A.D. Shaw, M. Amoozgar, M.I. Friswell, B.K.S. Woods, Bidirectional torsional negative stiffness mechanism for energy balancing systems, Mech. Mach. Theory 131 (2019) 261–277, https://doi.org/10.1016/j.mechmachtheory.2018.10.003.

[37] J. Zhang, A.D. Shaw, M. Amoozgar, M.I. Friswell, B.K.S. Woods, Bidirectional spiral pulley negative stiffness mechanism for passive energy balancing, J. Mech. Robot. 11 (2019), https://doi.org/10.1115/1.4043818.

[38] J. Zhang, A.D. Shaw, A. Mohammadreza, M.I. Friswell, B.K.S. Woods, Spiral pulley negative stiffness mechanism for morphing aircraft actuation, in: Vol. 5B 42nd Mech. Robot. Conf., American Society of Mechanical Engineers, 2018, V05BT07A003.

[39] S. Kumar, D. Komp, M. Hajek, J. Rauleder, Integrated rotor performance improvement and vibration reduction using active camber morphing, in: ASME 2019 Conf. Smart Mater. Adapt. Struct. Intell. Syst., American Society of Mechanical Engineers, 2019.

[40] D. Komp, S. Kumar, A. Abdelmoula, M. Hajek, J. Rauleder, Investigation of active rotor design and control for performance improvement, in: Vert. Flight Soc. - Forum 75 Futur. Vert. Flight - Proc. 75th Annu. Forum Technol. Disp., 2019.

[41] A. Abdelmoula, S. Platzer, M. Hajek, J. Rauleder, Numerical investigation of the effects of dynamic camber variation on the airfoil characteristics of a pitching rotor airfoil, in: AIAA Scitech 2020 Forum, American Institute of Aeronautics and Astronautics, Reston, Virginia, 2020.

[42] D. Wagg, S. Neild, Nonlinear vibration with control, Solid Mech. Appl. (2010), https://doi.org/10.1007/978-90-481-2837-2_1.

[43] P. Gudmundson, On the accuracy of the harmonic balance method concerning vibrations of beams with nonlinear supports, Ing.-Arch. (1989), https://doi.org/10.1007/BF00534063.